The High-Altitude MMIC Sounding Radiometer for the Global Hawk Unmanned Aerial Vehicle: Instrument Description and Performance

Shannon T. Brown, *Member, IEEE*, Bjorn Lambrigtsen, Richard F. Denning, *Senior Member, IEEE*, Todd Gaier, Pekka Kangaslahti, Boon H. Lim, Jordan M. Tanabe, and Alan B. Tanner

***Abstract*—The Jet Propulsion Laboratory's High-Altitude Monolithic Microwave Integrated Circuit (MMIC) Sounding Radiometer (HAMSR) is a 25-channel cross-track scanning microwave sounder with channels near the 60- and 118-GHz oxygen lines and the 183-GHz water-vapor line. It has previously participated in three hurricane field campaigns, namely, CAMEX-4 (2001), Tropical Cloud Systems and Processes (2005), and NASA African Monsoon Multidisciplinary Analyses (2006). The HAMSR instrument was recently extensively upgraded for the deployment on the Global Hawk (GH) unmanned aerial vehicle platform. One of the major upgrades is the addition of a front-end low-noise amplifier, developed by JPL, to the 183-GHz channel which reduces the noise in this channel to less than 0.1 K at the sensor resolution (∼2 km). This will enable HAMSR to observe much smaller scale water-vapor features. Another major upgrade is an enhanced data system that provides onboard science processing capability and real-time data access. HAMSR has been well characterized, including passband characterization, along-scan bias characterization, and calibrated noise-performance characterization. The absolute calibration is determined in-flight and has been estimated to be better than 1.5 K from previous campaigns. In 2010, HAMSR participated in the NASA Genesis and Rapid Intensification Processes campaign on the GH to study tropical cyclone genesis and rapid intensification. HAMSR-derived products include observations of the atmospheric state through retrievals of temperature, water-vapor, and cloud-liquid-water profiles. Other products include convective intensity, precipitation content, and 3-D storm structure.**

***Index Terms*—Airborne remote sensing, microwave sounder, tropical cyclone, unmanned aerial vehicle.**

I. Introduction

THE High-Altitude Monolithic Microwave Integrated Circuit (MMIC) Sounding Radiometer (HAMSR) is a cross-track scanning atmospheric sounder which was designed and built at the NASA Jet Propulsion Laboratory under a grant from the NASA Instrument Incubator Program in 2001. Beginning in 2008, HAMSR was extensively upgraded under the NASA Airborne Instrument Technology Transfer program to deploy on the NASA Global Hawk (GH) platform and serve as an asset to the NASA suborbital program. The HAMSR instrument was originally designed to be similar to the Advanced Microwave Sounding Units (AMSU) on the NOAA environmental satellites and has many of the same channels as AMSU. HAMSR has eight sounding channels near the 60-GHz oxygen-line complex, ten channels near the 118.75-GHz oxygen line, and seven channels near the 183.31-GHz water-vapor line.

HAMSR was first deployed in the field in the 2001 Fourth Convection and Moisture Experiment (CAMEX-4)—a hurricane field campaign operating out of Jacksonville, FL. HAMSR also participated in the Tropical Cloud Systems and Processes (TCSP) hurricane field campaign operating out of Costa Rica in 2005. In both of these campaigns, HAMSR flew as one of the payloads on the NASA high-altitude ER-2 aircraft. HAMSR flew on the NASA DC-8 during the NASA African Monsoon Multidisciplinary Analyses campaign, which took place in 2006 and operated from Cape Verde, Africa.

Since these campaigns, the HAMSR instrument has been upgraded to dramatically improve the receiver performance and to consolidate the instrument into a compact package. This includes the addition of state-of-the-art low-noise amplifiers (LNAs), in terms of gain and noise temperature, to the 118- and 183-GHz receivers. Another significant upgrade was the addition of a networked Linux data system, making possible real-time data access through the GH data network. This is important because of the long-duration—up to 30 h—GH flights. HAMSR data are transmitted to the ground in near real time, where it is processed and distributed to users during the flight.

After completion of the instrument upgrades, an extensive calibration and characterization campaign was conducted. This included measurements of the end-to-end frequency response of the system, an along-scan bias characterization, and a characterization of measurement noise of the calibrated brightness temperatures. The absolute calibration is best estimated in-flight through comparisons to modeled brightness temperatures generated using coincident radiosonde observations.

A main application for HAMSR data is to retrieve the thermodynamic state of the atmosphere through 3-D temperature and water-vapor profiles as well as cloud liquid water. Because of its profiling capability, HAMSR is also valuable for observations of the precipitation structure of storms. In past hurricane field campaigns, HAMSR data have been used to reveal both the precipitation structure of several mature hurricanes as well

Manuscript received July 1, 2010; revised December 10, 2010 and January 27, 2011; accepted February 6, 2011. Date of publication April 19, 2011; date of current version August 26, 2011.

The authors are with the NASA Jet Propulsion Laboratory, California Institute of Technology, Pasadena, CA 91109 USA (e-mail: Shannon.T.Brown@jpl.nasa.gov; bjorn.lambrigtsen@jpl.nasa.gov; richard.denning@jpl.nasa.gov; Todd.gaier@jpl.nasa.gov; pekka.kangaslahti@jpl.nasa.gov; Boon.Lim@jpl.nasa.gov; jordan.tanabe@jpl.nasa.gov; Alan.Tanner@jpl.nasa.gov).

Color versions of one or more of the figures in this paper are available online at http://ieeexplore.ieee.org.

Digital Object Identifier 10.1109/TGRS.2011.2125973

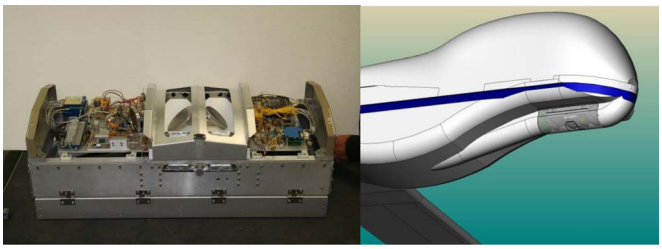

Fig. 1. Images of the (left) HAMSR instrument and (right) its deployment location on the GH.

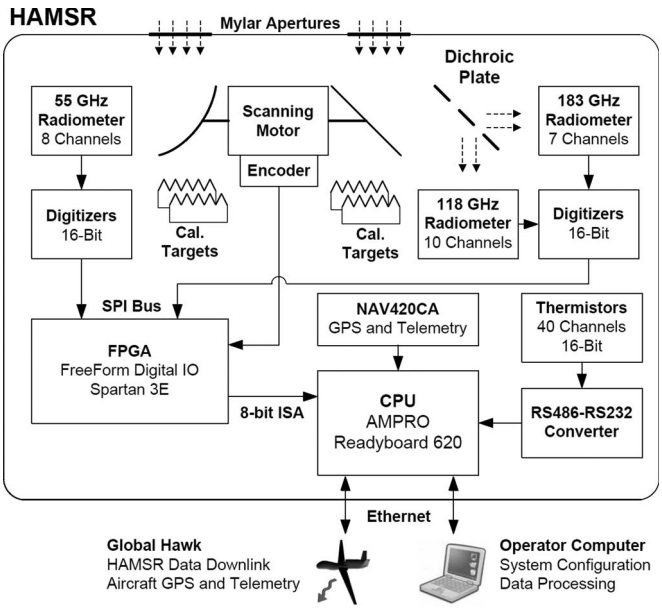

Fig. 2. HAMSR system-level block diagram.

as the structure of the warm core anomaly, both of which are related to storm intensity [1].

II. Instrument Description

The HAMSR instrument, shown in Fig. 1, is designed to fit in a small unpressurized downward-facing space within a wing pod or the fuselage of an aircraft. For the NASA GH aircraft, it is deployed in a forward bay (Zone 3) under the nose of the aircraft. The HAMSR instrument is contained within a compact package measuring 90 cm long, 38 cm wide, and 33 cm tall and weighing approximately 45 kg. The instrument is a downward-looking cross-track scanner with a scan axis that is oriented along the aircraft flight path. A system diagram is shown in Fig. 2.

The HAMSR receiver system consists of three MMIC-based heterodyne spectrometers covering three bands near 50, 118, and 183 GHz. The antenna system consists of two back-to-back reflectors which rotate together at a programmable scan rate via a stepper motor. A single full rotation includes the swath below the aircraft followed by observations of ambient (roughly 0 °C in flight) and heated (70 °C) blackbody calibration targets which are located at the top of the rotation. An FPGA is used to read the digitized radiometer counts and receive the reflector position from the scan motor encoder, which are then sent to a microprocessor and packed into data files. The microprocessor additionally reads telemetry data from 40 onboard housekeeping channels (containing instrument temperatures) and receives packets from an onboard navigation unit, which provides GPS time and position, as well as independent attitude information (e.g., heading, roll, pitch, and yaw). The raw data files are accessed through an Ethernet port. The HAMSR data rate is relatively low, at 75 kb/s, allowing for real-time access over the GH high-data-rate downlink. Once on the ground, the raw data are unpacked and processed though two levels of processing. The Level 1 product contains geolocated time-stamped calibrated brightness temperatures for the earth scan. These data are then input to a 1-D variational retrieval algorithm to produce temperature, water-vapor, and cloud-liquid-water profiles, as well as several derived products, such as potential temperature and relative humidity [1].

A. Antenna/Scan System

The HAMSR antenna scan system consists of two rotating mirrors: one parabolic reflector for the 50–57-GHz channels and one flat plate for the 113–119- and 166–193-GHz channels, which are mechanically connected to a common scan motor and rotate about a single axis. A detailed description of the HAMSR antenna system is found in [14] and summarized here. Each reflector is fed by circular corrugated horns with a 16-dB reflector edge taper. The 118- and 183-GHz signals are split after the flat reflector using a dichroic plate that is centered along the scan axis. The dichroic plate splits these two bands toward respective parabolic reflectors which focus the beam into the two respective receivers. This design provides matched and coincident antenna beams in all three RF bands. The size of the beam at each band is 5.7° half power full width (HPFW), and the sidelobes for all beams for angles greater than 10° off boresight are well below 30 dB with a beam efficiency of $> 95\%$ (defined as the fraction of power received within 2.5 times the main beamwidth), providing minimal footprint contamination. From a flight altitude of 20 km, the beamwidth corresponds to a 2-km footprint on the ground at nadir. The polarization of the beams rotates as the reflectors scan, with pure V-polarization at nadir. The unobstructed cross-track swath spans $\pm 45°$ from nadir, giving a 40-km swath from a 20-km flight altitude. Past 45°, the edge of the aperture begins to intersect the beam, but the data may still be useable out to $\pm 60°$ depending on the error tolerance of the particular application. A characterization of scan-dependent biases is given in Section III-B.

Each reflector observes two pyramidal blackbody calibration targets during each scan that are located on the top of the scan arc. One target is at the ambient air temperature (cold at altitude), and the other is heated to about 70 °C. The targets were procured commercially and designed to have more than 50-dB return loss from 40 to 220 GHz. The targets are about 16 × 12 cm in area with 4-cm-long pyramids separated at the tips by 1 cm. The pyramids are constructed from heavy aluminum and coated with a ferrite-loaded epoxy-absorbing material. The ambient and hot targets are identical for the 50- and 118/183-GHz sides. The temperature of each target is measured with four temperature sensors embedded within the target near the tips. The targets are insulated with Styrofoam to keep thermal gradients minimal. The spatial thermal gradients horizontally across both targets, measured using the four embedded thermistors, show that the gradients in flight are less

than 0.25 K. The Styrofoam radome covers the pyramids and is between the antenna and the load. The Styrofoam is 0.7 cm thick and has a measured loss that ranges from 0.04% at 50 GHz to 0.15% at 183 GHz. The return loss of the Styrofoam is > 37 dB at all HAMSR frequencies. Assuming that the effective brightness of the reflected contribution is within about 100 K of the target temperature, which is a reasonable assumption for observations where the incidence angle on the Styrofoam is off normal, then the dominant error term is due to the ohmic loss component. It should be noted that the observations where the Styrofoam is normal to the beam are excluded when computing the average calibration target counts to avoid local-oscillator reflections and coherent receiver noise biasing the calibration measurement. Because the temperature of the ambient target and the Styrofoam are nearly equivalent, the error due to the Styrofoam over the ambient target is negligible. If we assume that the Styrofoam temperature is at the instrument frame temperature in flight (measured to be 263 K at minimum), then the maximum error looking at the 343 K calibration target due to the foam is 0.04 K at 50 GHz and 0.1 K at 183 GHz.

The instrument external aperture is covered by a 0.0127-mm-thick (0.5-mil) Mylar radome on the 50-GHz side and a 0.0063-mm-thick (0.25-mil) Mylar radome on the 118/183-GHz side, which are used to limit condensation or frosting on the reflectors and Styrofoam covers by keeping the temperature near the targets higher than the outside ambient temperature. The instrument housing is warmed by the receiver subsystem baseplates, which are controlled to 30 °C. In flight, the instrument outer frame temperature reached a minimum of −10 °C, while the ambient air temperature was near −60 °C. The RF loss through the Mylar radome at 183 GHz is less than 0.1%, giving at most a 0.1-K error for typical brightness temperatures at a 20-km altitude.

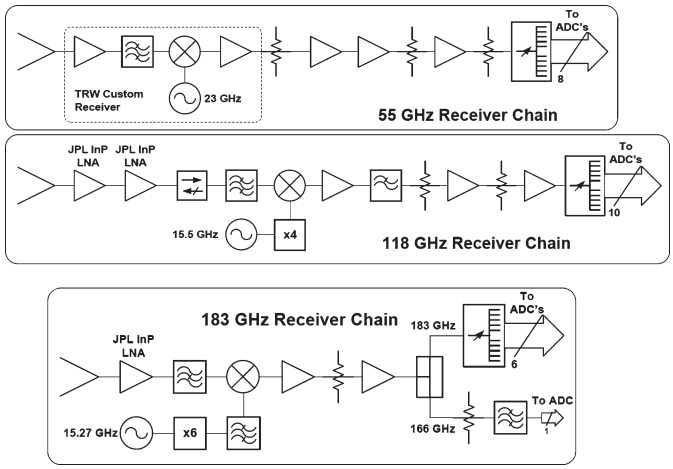

Fig. 3. HAMSR receiver block diagrams: (Top) 50 GHz, (middle) 118 GHz, and (bottom) 183 GHz.

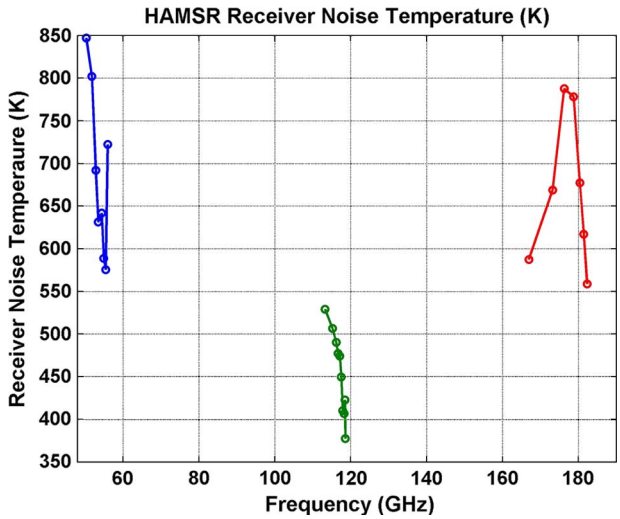

Fig. 4. Measured receiver noise temperature as a function of frequency for the HAMSR channels.

B. Receiver System

The HAMSR receiver system consists of three MMIC-based heterodyne receivers with very broad (up to 18 GHz) intermediate frequency (IF) outputs which are subsequently amplified and then multiplexed via filter banks into the 25 spectral channels. The power in each channel is detected, integrated, and digitized simultaneously and then recorded by the data acquisition and control system. The HAMSR 118- and 183-GHz receiver systems were recently upgraded, taking advantage of the state-of-the-art high-frequency LNA development projects at JPL [2]. A block diagram of each receiver is shown in Fig. 3. All three receivers (55, 118, and 183 GHz) now employ InP MMIC RF LNA front ends. The 118- and 183-GHz LNAs were developed in 2007 at JPL under the MIMRAM Advanced Component Technology project, and HAMSR is the first science instrument to use this technology. These LNAs provide state-of-the-art noise performance and give a significant performance improvement over the previous receivers. The 183-GHz receiver benefited the most since a conventional planar mixer–receiver—with more than 8000-K receiver noise—was replaced with an LNA front end with less than 600-K receiver noise. The measured receiver-noise temperatures (measured through the entire system), shown in Fig. 4 for each channel, are between 550 and 850 K at 50 GHz, 350 and 550 K at 118 GHz, and 550 and 800 K at 183 GHz. Low noise performance is crucial for sounding applications and even more so when observing at small spatial scales from a moving platform. HAMSR is now able to resolve fine-scale spatial structures in the atmosphere which were previously masked by receiver noise.

All components of the receiver system are mounted to a common aluminum baseplate, one for the 50-GHz side and one for the 118/183-GHz side. The RF components are mounted on the side of the plate facing the antenna aperture and are insulated with a foam cover. Each plate is controlled to 30 °C using heaters with a thermostat control. Fans, mounted in the side wall of the instrument housing, are used to cool the instrument by blowing external air across the exposed back side of the plates when the plate temperature exceeds 30 °C. When the outside air temperature exceeds 35 °C, the instrument can only operate for a few hours before the components reach their upper temperature limits. In flight, the thermal system is able to maintain the baseplate temperature at 30 °C.

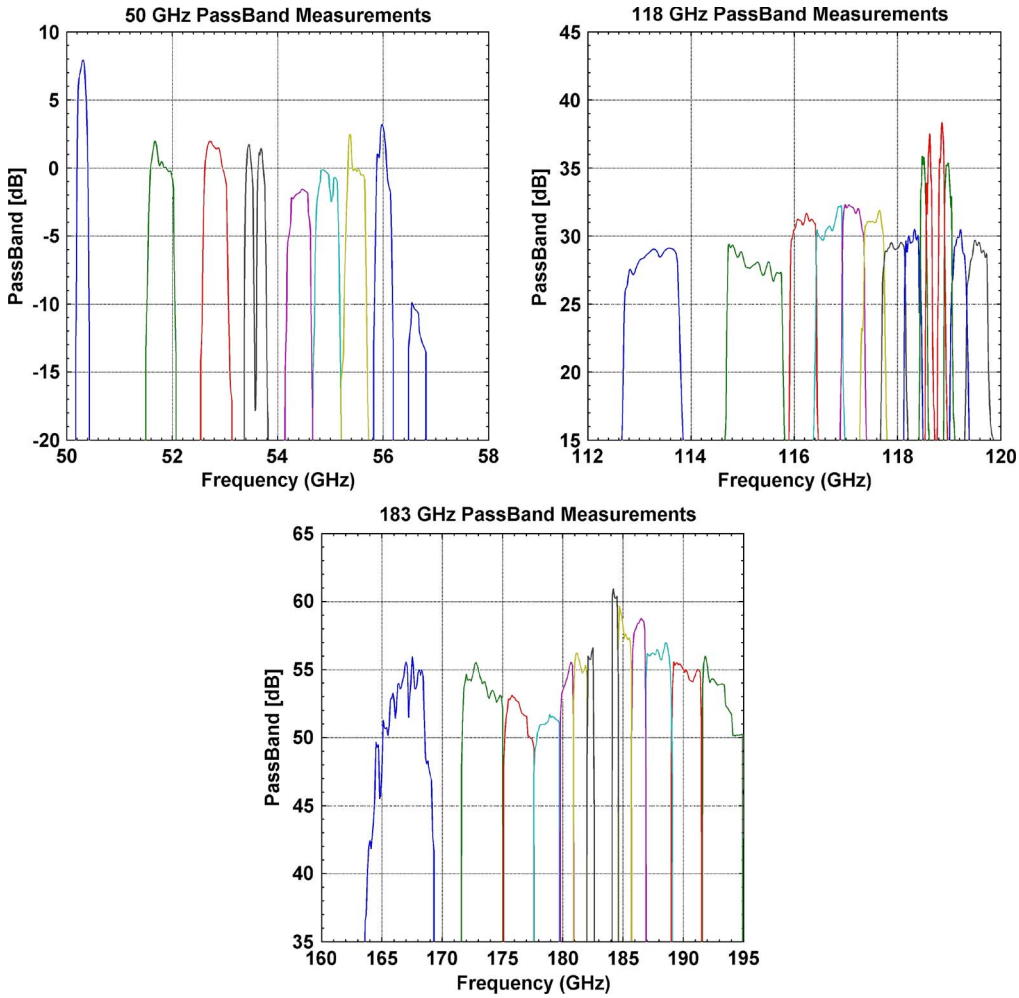

Fig. 5. (Top left) 50-GHz, (top right) 118-GHz, and (bottom) 183-GHz HAMSR passband measurements.

III. HAMSR Calibration and Characterization

After completion of the HAMSR system upgrades, a calibration and characterization effort was conducted. The objectives were to accurately measure the end-to-end frequency response of the system, assess potential scan-dependent biases, and characterize the system stability to optimize the scan rate and minimize measurement noise. These tests and results are described in the following sections.

A. HAMSR Frequency Response

Accurate characterization of the end-to-end frequency response of the system is critical for geophysical retrievals and data assimilation due to the significant spectral variability of the scene within and across the HAMSR channels. The passbands were measured at the input of the receiver just beyond the feedhorn. The feedhorn, and the rest of the optical system, was measured separately and found to be sufficiently broadband and well matched ($>$ 20 dB) to have little impact on the end-to-end receiver passband. To get the HAMSR end-to-end receiver gain as a function of frequency for each channel, an upconverted signal from an RF synthesizer was swept across the HAMSR bands and measured with a power meter at the IF output port just before the detector. An attenuator was placed between the RF source and receiver to protect the LNAs and make the measurements in a linear regime of the amplifiers. The power gain transfer function $G(f)$ is computed from the measurements as

$$G(f) = \frac{P_{\text{out}}(f)}{P_{\text{in}}(f)} = \frac{P_{\text{out}}(f)}{P_{\text{src}}(f)A(f)} \tag{1}$$

where $P_{\text{out}}(f)$ is the power measured by the power meter at the IF output port, $P_{\text{src}}(f)$ is the power of the source that was measured after the upconversion stage, and $A(f)$ is the broadband attenuator that is placed between the source and the radiometer. The attenuator was characterized separately using a Vector Network Analyzer since the power meter used to characterize RF output power was not sensitive enough with the attenuator connected. The source power and attenuator were observed to be nearly flat over the HAMSR passbands, making errors in the characterization of their spectral response negligible in the final HAMSR passbands. The passbands measured for the 25 HAMSR channels are shown in Fig. 5. From these data, the channel centroid frequency, convolution bandwidth, and sideband weighting ratio are computed. These values are given in Table I for each channel and for the upper and lower sidebands separately for the double-sideband channels. The sideband weighting ratio is the ratio of the power

TABLE I
HAMSR FREQUENCY RESPONSE: CENTROID FREQUENCY, BANDWIDTH, AND UPPER/LOWER SIDEBAND WEIGHTING

Channel	f_c – LSB [GHz]	BW – LSB [MHz]	W_1	f_c – USB [GHz]	BW – USB [MHz]	W_2
1	50.30	185.34	-	-	-	-
2	51.81	456.26	-	-	-	-
3	52.82	444.60	-	-	-	-
4	53.46	151.29	0.58	53.69	155.73	0.42
5	54.41	446.50	-	-	-	-
6	54.94	442.91	-	-	-	-
7	55.46	374.80	-	-	-	-
8	55.99	279.05	0.90	56.61	235.84	0.10
9	113.27	1062.11	-	-	-	-
10	115.19	1060.03	-	-	-	-
11	116.18	506.09	-	-	-	-
12	116.70	504.33	-	-	-	-
13	117.13	432.13	-	-	-	-
14	117.54	418.95	-	-	-	-
15	117.93	459.60	0.54	119.56	424.56	0.46
16	118.30	319.84	0.54	119.19	302.38	0.46
17	118.50	117.19	0.47	118.98	140.74	0.53
18	118.61	100.86	0.42	118.86	105.95	0.58
19	166.95	3812.82	-	-	-	-
20	173.22	3298.97	0.54	192.88	2926.96	0.46
21	176.26	2409.16	0.34	190.23	2472.45	0.66
22	178.74	2133.24	0.23	187.95	2162.90	0.77
23	180.39	1093.10	0.29	186.32	1119.17	0.71
24	181.44	1157.75	0.36	185.09	1109.80	0.64
25	182.30	536.28	0.27	184.31	539.22	0.73

received in one sideband to the total power received for that channel (e.g., from both sidebands). The centroid frequencies and bandwidths for all the channels were found to be very close to the original design specifications. The rejection of the 166-GHz channel upper sideband, provided by an RF image reject filter, was found to be greater than 25 dB. Because the end-to-end passbands can change with temperature, the passband measurements were made with the instrument active thermal control at its nominal in-flight setpoint. The temperature of the components critical to defining the passband shape was within a few degrees (generally less than 3 °C) during the test as they are in flight.

B. Scan Bias Characterization

A common issue with microwave imagers is a calibration bias that is dependent on the antenna scan position. The bias results because the antenna sidelobe contributions are slightly different for each position in the scan and these contributions are not removed by the onboard blackbody calibration. In the case of HAMSR, a bias can result from the portion of the beam that spills over onto the metal frame around the scan arc. The frame was sized to minimize this error as much as possible, but some effect is inevitable, particularly at the scan edges. A special test was conducted to assess any scan-dependent biases in the HAMSR image. The test was done outside on a clear and calm day and was designed to reveal scan biases relative to the nadir position. It should be noted that a spill-over bias common to all scan positions, and thus impacting the overall absolute calibration, would not be detected by this test. An assessment of the HAMSR absolute calibration is discussed in Section III-D. HAMSR was positioned to view toward zenith, scanning an arc across the sky. The instrument was then rotated in the plus and minus direction along the direction of the scan using a special rotation fixture so that the sky zenith was viewed at each scan position. The instrument was rolled in increments of 5°, and the roll angle was accurately measured using HAMSR's onboard navigation system with an accuracy of better than 0.05°. The scan bias was computed by taking the difference of the zenith measurement at each scan position relative to the measured zenith value at center scan position when the roll was zero

$$\Delta T_B(\theta_H) = T_B\left(\{\theta_{\text{Roll}} = 0^\circ, \theta_H = 0^\circ\}\right) - T_B\left(\{\theta_{\text{Roll}} - \theta_H\} = 0^\circ\right) \quad (2)$$

where θ_{Roll} is the roll angle of the instrument and θ_H is the scan angle of the HAMSR antenna. The HAMSR scan angle is defined to be zero at the center of the scan, and the roll angle is defined to be zero when the center of the scan points at the sky zenith. The main assumption for the test is that the sky temperature is constant over the measurement period. To avoid changes in the sky impacting the measurement, the test was conducted over a period of 15 min and repeated several times.

The results for each channel are shown in Fig. 6 for scan angles between $\pm 60^\circ$ from the center scan position. No significant scan bias is observed in any channel between $\pm 45^\circ$. In the 50-GHz channels, the bias is observed to be less than 0.8 K for scan angles between $\pm 45^\circ$, and for the 118/183-GHz channels, the bias is observed to be less than 0.5 K over this scan range. It is clear that most of the spillover energy received is from the inside of the instrument near the ambient instrument temperature since the observed biases in Fig. 6 scale with scene temperature, giving a larger bias for the more transparent channels that diminishes for the more opaque channels. The zenith brightness temperature during the test was near 70 K at 50.3 GHz, 80 K at 113.27 GHz, and 138 K at 166.95 GHz. From these measurements and the assumption that the spillover is largely independent of frequency within a band, we can bound the spillover contribution within $\pm 45^\circ$ of the scan center to be less than 0.35% for the 50-GHz channels and less than 0.32% for the 118/183-GHz channels. At a flight altitude of 20 km and excluding extreme scattering events, the brightness temperatures are typically no less than 150 K for any channel, making the worst case error no greater than 0.5 K and typically on the order of 0.25 K. It should also be noted that this error is mostly confined to the edge of the scan where the metal frame occupies more of the field of view.

C. System Stability/NEDT Optimization

The noise on the calibrated brightness temperature measurement as a function of the integration time on the scene τ_A and the integration time on calibration measurements τ_{Cal} can be represented as the root sum square (RSS) of three terms: the

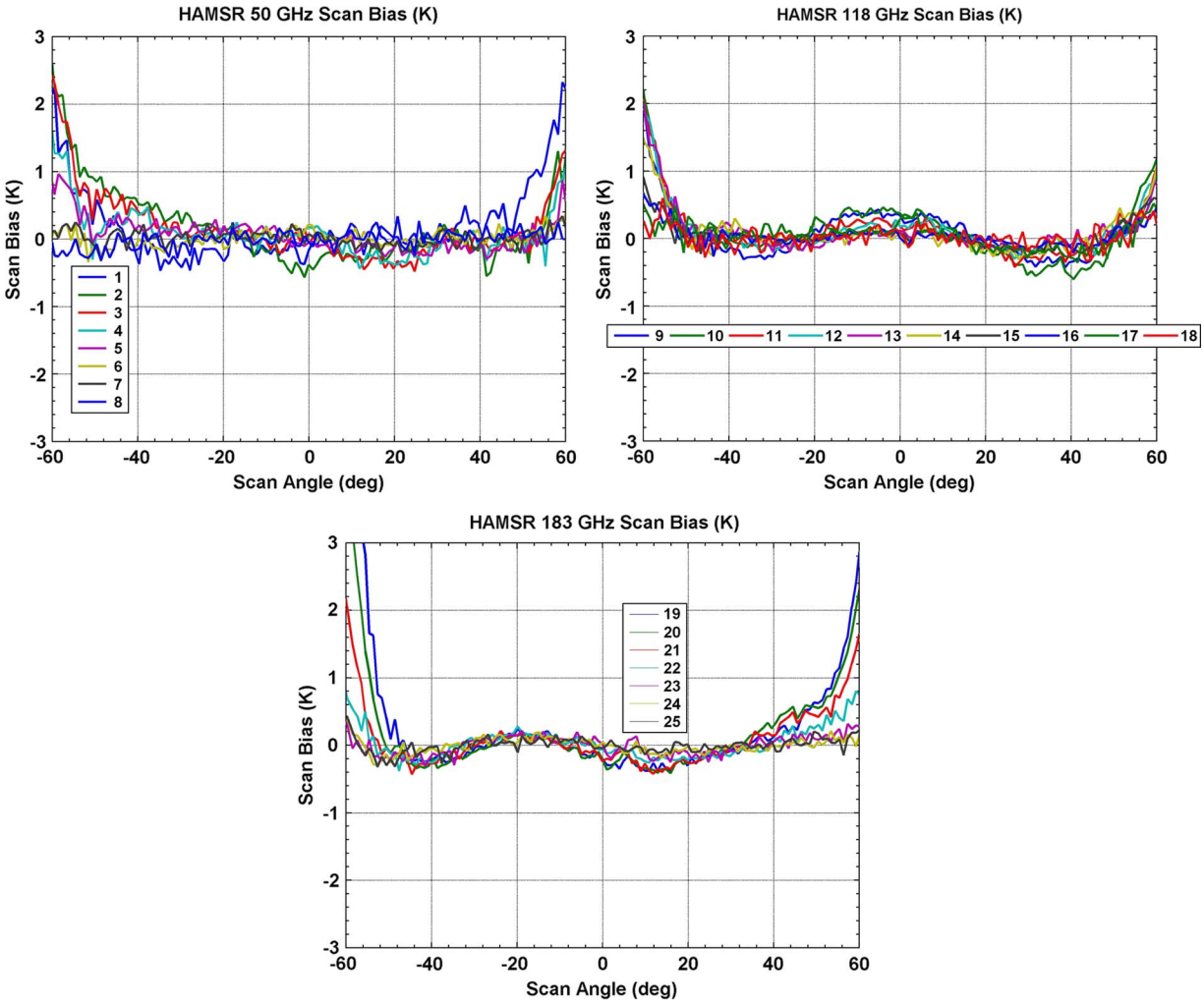

Fig. 6. Relative scan bias for the HAMSR instrument for each channel.

noise on the antenna measurement, the white noise on the calibration measurements which decreases with increasing integration time, and the systematic noise ($1/f$ noise) which increases with increasing integration time

$$\Delta T_A^2(\tau_A, \tau_{\rm Cal}) = \left\{ NE\Delta T^2(\tau_A) + \Delta T^2_{\rm Cal\_white}(\tau_{\rm Cal}) + \Delta T^2_{\rm Cal\_Systematic}(\tau_{\rm Cal}) \right\}. \quad (3)$$

We seek to minimize the contribution of the last two terms in (3) to the overall measurement noise. A running average of several scans of calibration measurements centered on the scene measurement is used to increase the integration time of the calibration measurements to reduce the white-noise component of calibration at the expense of increasing the noise from systematic system drift over this time window. The system stability defines the maximum length of the running-average window. The scan consists of a slew across the Earth scene at a programmable scan rate, a dwell on the ambient target, and a dwell on the hot target, with rapid steps in between. The integration time is programmable and is nominally set to 7 ms. The Earth scene scan rate and target dwell time are set to minimize the effective noise equivalent delta temperature (NEDT) utilizing measurements of receiver stability and are constrained by a requirement for Nyquist sampling in the cross- and along-track directions. To assess the stability of the HAMSR receivers, the instrument was configured to stare at a blackbody target cooled with liquid nitrogen. The counts were scaled to brightness temperature using a constant gain and offset, computed from a previous test when the instrument was fully scanning and thus calibrated with the onboard calibration targets. From these data, the NEDT versus integration time was computed for each channel to assess the time period for which the systematic $1/f$ noise dominates over white noise. An example from each channel is shown in Fig. 7. In general, the 183-GHz receiver was found to have the best stability, followed by the 118-GHz receiver and the 50-GHz receiver. While the systematic noise begins to dominate the white noise on time scales of about 1 s, it only becomes significant compared with the minimum NEDT at time scales longer than this. At 50 GHz, systematic $1/f$ noise becomes significant past about 30 s of integration time; at 118 GHz, it becomes significant past 60 s; and at 183 GHz, it becomes significant past 100 s of integration time. Assuming a temperature difference between the hot target and ambient target of 70 °C, which is typical at flight altitude, it can be shown that the white noise on the calibration measurements reduces to a negligible level (e.g., contributing

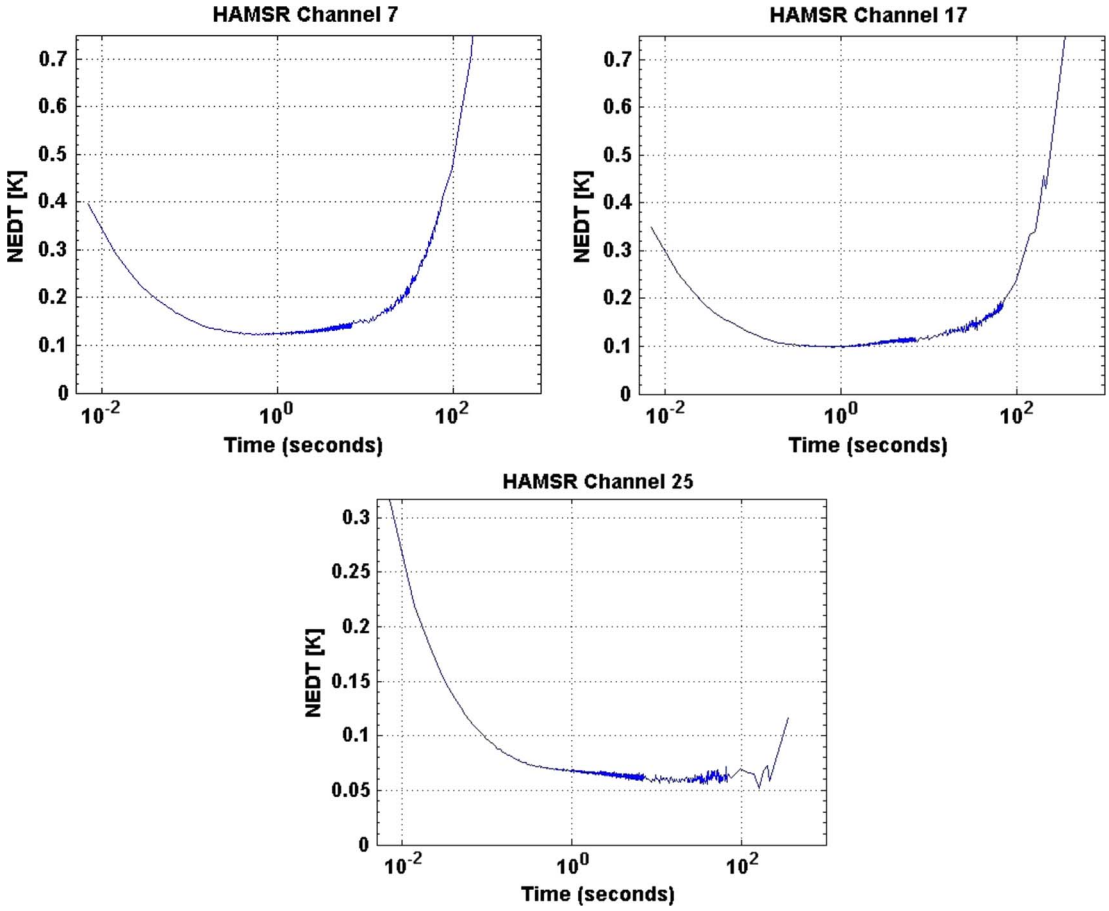

Fig. 7. HAMSR NEDT versus integration time for representative channels from each receiver chain.

less than 4% excess noise to the NEDT) after about 3 s of integration time on the calibration targets for the worst case channel (channel 1). For the nominal scan profile, the slew across the Earth scene, $\pm 60^\circ$ about nadir, is set to a scan rate of $120^\circ/\text{s}$ and the dwell on the calibration targets is set to 0.5 s each, giving a 2.2-s repeat cycle. With a 7-ms integration time, the beam center moves by 0.84° (14% of the HPBW) during the integration period, minimizing the smearing of the beam during the integration. For this scan profile, a minimum running-average-window length of six scans is needed to reduce the white noise on the calibration measurements to a negligible level. It takes 13.2 s to complete six scans, which is short enough so that systematic noise would not be significant for any of the receivers. In flight, for 2-km pixels, four samples are averaged in the along-track direction and three samples in the cross-track direction, giving a total integration time per sample of 0.084 s. To measure the NEDT of the calibrated brightness temperatures, the instrument was configured to scan across a stable 300-K blackbody target. The brightness temperature was computed using a 6-s along-track running average of the calibration measurements and a 4×3 pixel average on the target. From these data, the NEDT was computed and is shown in Table II, which represents the NEDT for a 300-K antenna temperature for a 2-km sample in-flight from the GH cruising altitude of 20 km. The measured HAMSR NEDTs at 300 K are between 0.16 and 0.3 K at 50 GHz, 0.1 and 0.15 K at 118 GHz, and 0.06 and 0.1 K at 183 GHz.

TABLE II
MEASURED HAMSR NEDT FOR AN EQUIVALENT 2-km PIXEL FROM 20 km

Channel	NEDT [K]	Channel	NEDT [K]	Channel	NEDT [K]
1	0.29	**10**	0.12	**19**	0.06
2	0.22	**11**	0.10	**20**	0.07
3	0.18	**12**	0.14	**21**	0.09
4	0.19	**13**	0.13	**22**	0.09
5	0.17	**14**	0.14	**23**	0.10
6	0.16	**15**	0.13	**24**	0.10
7	0.16	**16**	0.10	**25**	0.10
8	0.19	**17**	0.10		
		18	0.15		

D. In-Flight Absolute Calibration

The HAMSR absolute calibration is best assessed in-flight, since many of the error sources contributing to the absolute calibration error are dependent on flight conditions. For example, a dominant error arises from uncertainties in the calibration target temperature, which will be different in flight than in the laboratory, since the targets will exhibit different gradients in the cold turbulent flight environment compared with those obtained in the laboratory. The error due to calibration-target-temperature knowledge uncertainty is estimated to be less than 0.5 K. Other errors previously discussed and estimated were

TABLE III
HAMSR AVERAGE COMPARISON WITH THE MODEL FOR THE OPAQUE CHANNELS DURING AIRCRAFT ASCENT AND DESCENT

Chan #	Center freq. [GHz]	Avg Model – Measured Rosenkranz (1998) [K]	Std Model – Measured Rosenkranz (1998) [K]	Avg Model – Measured Liebe (1993) [K]	Std Model – Measured Liebe (1993) [K]
5	54.41	-0.20	0.75	-0.17	0.74
6	54.94	0.19	0.62	0.17	0.62
7	55.46	0.03	0.83	-0.01	0.83
8	55.99	-1.4	1.0	-1.4	1.1
16	118.30	1.1	1.2	0.82	1.2
17	118.50	0.83	1.2	0.26	1.2
18	118.61	1.2	1.2	0.47	1.3
23	180.39	0.50	2.4	0.06	2.4
24	181.44	-0.19	2.3	-0.43	2.3
25	182.30	0.20	2.4	0.13	2.3

errors due to the calibration target covers (< 0.1 K), errors due to the Mylar radome (< 0.1 K), and scan-dependent biases (< 0.5 K).

A technique was developed during TCSP to assess the absolute calibration of the HAMSR T_B's using the measurements taken during the ascent after takeoff and the descent before landing. For the channels near the absorption line, the surface is obscured and the measured brightness temperature as a function of height will trace out a smoothed version of the temperature profile, allowing one to assess gain, offset, and linearity errors. During the TCSP flights, radiosondes (RaObs) were launched from the originating airport every 6 h. A radiative transfer model is used, with the upper air data from the RaObs, to model the HAMSR upwelling T_B's during takeoff and landing using

$$T_{\mathrm{UP}}(f,H,\theta) = \sec\theta \int_0^H \kappa_a(f,z')T(z') \times \exp\left(-\int_{z'}^{H} \kappa_a(f,z)\sec\theta dz\right) dz' \quad (4)$$

where κ_a is the atmospheric absorption coefficient at height z and frequency f, $T(z)$ is the vertical temperature profile, θ is the incidence angle, and H is the aircraft altitude. Note that (4) is only valid for the opaque channels where the surface contribution is obscured by the atmosphere. The Rosenkranz 1998 [3] and the Liebe 1993 [4] models are used to determine the atmospheric absorption coefficient using the temperature, pressure, and water-vapor profiles from the RaObs. A clear atmosphere is assumed. An example of the modeled (using Rosenkranz 1998) and measured T_B's for the four highest 50-GHz channels for the ascending (shown in red) and descending (shown in blue) flight portions on July 28, 2005 is shown in Fig. 8 as a function of height from 1–20 km. For this analysis, only the nadir pixel is used. The large spikes in the measurements are due to aircraft maneuvers, pointing the nadir pixel at some slant path through the atmosphere.

Table III gives the average difference between the model and the measurements for the flights on July 5, 6, 9, 15, 16, 17, 23, 25, 27, and 28, 2005 between flight altitudes of 6–16 km. The ascending and descending data are averaged together in the table. The data near the surface were excluded to mitigate the error from an unknown surface emissivity. The data near the tropopause were excluded because of the decreased accuracy of the RaOb measurements at this altitude and because of the fact that, in general, these measurements were spatially farthest from the RaOb launch site. There is good agreement between the model and the measurements for the opaque HAMSR channels. The measurements agree to better than 1 K, with the exception of channel 8. The uncertainty in the model comparison arises from errors in the absorption model, errors in the RaOb profiles, errors in the navigation data (altitude and attitude), and possible water condensation on the reflector cover during ascent/decent. Considering these error sources, the inherent uncertainty in the comparison can be estimated to be at approximately the 1-K level. If one assumes that potential calibration errors are common to all HAMSR channels, such as errors in the knowledge of the absolute calibration target temperature, one can infer that the absolute calibration accuracy of the channels not compared with the model (the more transparent channels) will be similar. Also, since the calibration system was not changed during the recent instrument upgrades, the TCSP comparisons can still be considered valid for the HAMSR on the GH and the absolute calibration should be no worse than during TCSP. It is conservatively estimated that the HAMSR absolute brightness temperature calibration is better than 1.5 K, which will be verified during GH flights using the same technique.

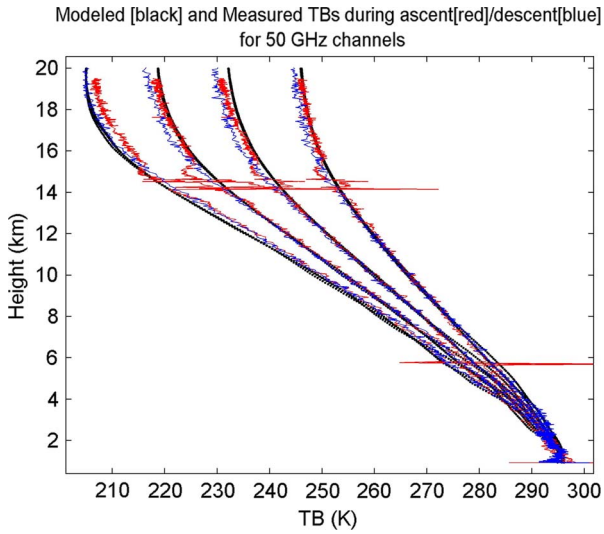

Fig. 8. HAMSR T_B's compared with those of the model for July 28, 2005. The red line denotes the ascending data, and the blue line shows the descending data.

IV. HAMSR APPLICATIONS

A. Monitoring the Thermodynamic State

A main application for the HAMSR instrument is monitoring the atmospheric state by retrieving 3-D profiles of temperature and water vapor at 2-km resolution from the GH cruising

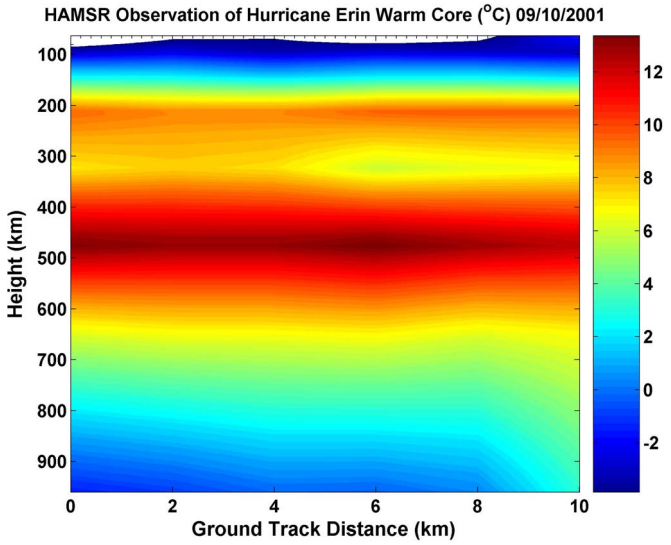

Fig. 9. HAMSR-derived warm core anomaly from Hurricane Erin on September 10, 2001.

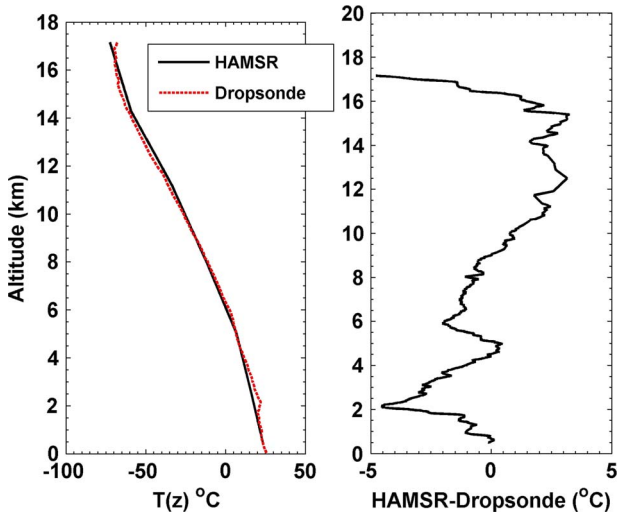

Fig. 10. HAMSR temperature profile compared with the dropsonde profile in the eye of Hurricane Erin.

altitude of 18–20 km. An optimal estimation-based retrieval algorithm developed for HAMSR has been used to derive profiles from past campaigns in which the instrument participated [1]. The focus of the previous HAMSR deployments has been on tropical cyclones. Of particular interest for monitoring tropical cyclone intensity is the observations of the warm core anomaly of the hurricane. The warm anomaly is found by differencing the temperature profile retrieved in the eye from an environmental profile retrieved away from the storm. Previous work has shown that the magnitude of the warm anomaly in the core of a tropical cyclone can be used to predict the central pressure and maximum surface winds of the storm [5]–[7]. Using AMSU, a linear relationship is found between the 200-mb warm anomaly and maximum wind speed of 8 kt/K and a similar relationship to central pressure depression below 1013 mb of 6.3 mb/K. On the GH, there is the possibility of long-duration reconnaissance near the eye to provide continuous monitoring of the evolution of hurricane intensity.

During CAMEX-4 and TCSP, the ER-2 was fortunate enough to fly over the eye of two mature hurricanes. Fig. 9 shows the warm core structure for Hurricane Erin on September 10, 2001 derived from HAMSR measurements. The maximum magnitude of the warm anomaly peaks near 11 °C–12 °C. The warmest temperatures for Hurricane Erin occur between 400 and 600 mb. A comparison between the HAMSR temperature profile in the eye and a dropsonde temperature profile is shown in Fig. 10 [8]. The differences between the HAMSR-derived profile and the dropsonde profile are small (generally less than 1 °C).

In addition to being able to monitor hurricane intensity over time periods exceeding 24 h, significant improvements could be made to AMSU algorithms which suffer from the low spatial resolution of AMSU. The long duration of the unmanned aerial vehicle–HAMSR observations on the GH would virtually guarantee several AMSU overpasses, which will provide a clear high-resolution image of the storm by which the satellite algorithms can be improved.

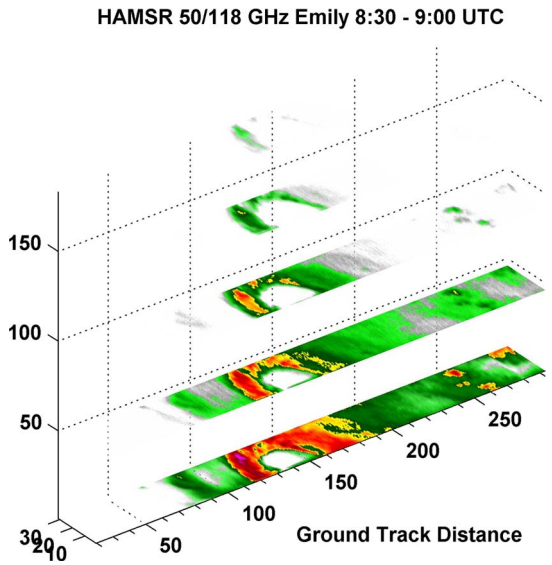

Fig. 11. HAMSR vertical slices of 50/118-GHz T_B differences for Hurricane Emily. The slices represent precipitation intensity above approximately 0, 4, 8, 12, and 15 km with green qualitatively representing less intense precipitation and red to purple indicating more intense precipitation.

B. Precipitation Structure

The profiling capability of the HAMSR channels is also valuable for monitoring the 3-D precipitation structure of the tropical cyclone. This is because the weighting functions for the channels peak at different altitudes in the atmosphere and are thus sensitive to different levels in the storm, mainly through the scattering signature of the precipitation. There are two approaches that have been applied to HAMSR data. The first applies a "cloud-slicing" technique, making use of the 50- and 118-GHz channels which have matched clear-air weighting functions [9]–[11].

In clear air, these 50/118-GHz channel pairs will have essentially no brightness temperature difference between them, but in the presence of precipitation, the 118-GHz channels will

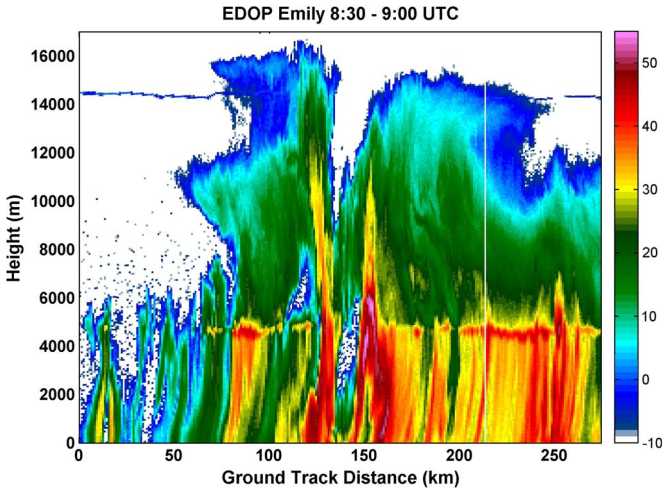

Fig. 12. Nadir reflectivity of Hurricane Emily from EDOP on ER-2.

see significantly more scattering from the precipitation, leading to large differences proportional to the precipitation intensity. Because the weighting functions for the channel pairs peak at different vertical locations in the atmosphere, a precipitation profile can be obtained. This is shown in Figs. 11 and 12. Fig. 11 shows five slices through Hurricane Emily where the slices indicate the qualitative precipitation intensity above 0, 4, 8, 12, and 15 km. Fig. 12 shows the vertical reflectivity profile from the ER-2 Doppler (EDOP) radar on the ER-2. The asymmetrical structure of the storm is evident in the HAMSR slices, particularly the convective tower peaking above 15 km on the left side of the figure (western side of the eye).

The second approach uses the full complement of the HAMSR T_B's to derive equivalent radar reflectivity profiles using a regression algorithm similar to those that have been applied to AMSU/HSB data [12], [13]. This is shown in Fig. 13, which shows derived reflectivity slices from 2 to 15 km over Hurricane Emily, providing a qualitative view of the precipitation structure of the storm. This algorithm was trained using several flights from the TCSP campaign in which the EDOP and HAMSR flew on the ER-2.

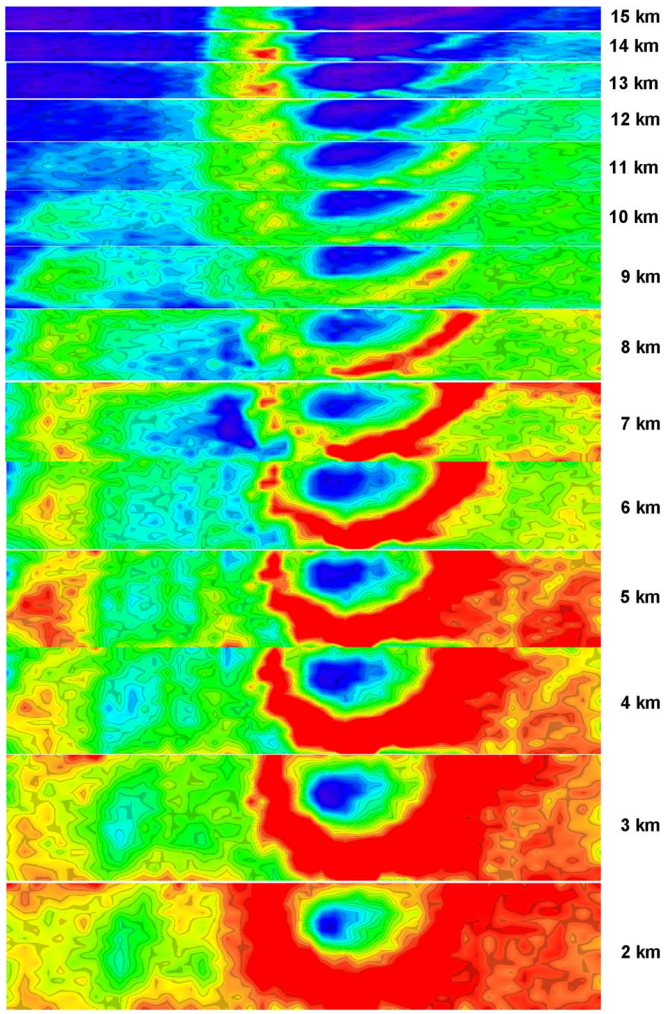

Fig. 13. Equivalent radar reflectivity slices derived from HAMSR T_B's for Hurricane Emily with blue to green qualitatively representing less intense precipitation and yellow to red indicating more intense precipitation.

V. Summary and Future Work

The HAMSR instrument, which began as an Instrument Incubator Program technology demonstration, has been upgraded to serve as a reliable operational asset to suborbital science programs. The addition of a state-of-the-art LNA to the 183-GHz receiver front end and the upgrade of the 118-GHz LNA provide excellent low-noise performance which is critical for microwave sounding retrievals. The data system is upgraded to provide in-flight data access through the GH data link, making it possible to relay data to the ground in real time. This is particularly relevant for hurricane observations where HAMSR can provide real-time information on tropical storm structure, intensity, and evolution. After the completion of the instrument upgrades, the HAMSR instrument calibration and performance were well characterized. This included characterization of the end-to-end HAMSR passbands, an along-scan bias characterization, and measurement noise characterization. The HAMSR absolute calibration is validated in-flight, using data taken during the aircraft ascent and descent from the originating airport and comparing them with a radiative transfer model fed by upper air sounding data from a coincident radiosonde observation. This analysis was done during a previous campaign, and the HAMSR absolute calibration is conservatively estimated to be better than 1.5 K. The HAMSR instrument flew on the GH for the NASA Genesis and Rapid Intensification Processes campaign between August 15 and September 30, 2010. Following this campaign, HAMSR will fly on the GH during the Hurricane and Severe Storms Sentinel campaign, under the NASA Earth Science Ventures program, which is scheduled for flights during the 2012–2014 hurricane seasons.

Acknowledgment

The work described in this paper was performed at the NASA Jet Propulsion Laboratory, California Institute of Technology, under a contract with the National Aeronautics and Space Administration.

REFERENCES

[1] S. Brown, B. Lambrigtsen, A. Tanner, J. Oswald, D. Dawson, and R. Denning, "Observations of tropical cyclones with a 60, 118 and 183 GHz microwave sounder," in *Proc. IGARSS*, Jul. 23–28, 2007, pp. 3317–3320.

[2] P. Kangaslahti, D. Pukala, T. Gaier, W. Deal, X. B. Mei, and R. Lai, "Low noise amplifier for 180 GHz band," in *Proc. IEEE Int. Microw. Symp.*, Jun. 2008, pp. 451–454.

[3] P. Rosenkranz, "Water vapor microwave continuum absorption: A comparison of measurements and results," *Radio Sci.*, vol. 33, no. 4, pp. 919–928, Jul./Aug. 1998.

[4] H. Liebe, G. A. Hufford, and M. G. Cotton, "Propagation modeling of moist air and suspended water particles at frequencies below 1000 GHz," in *Atmospheric Propagation Effects Through Natural and Man-Made Obscurants for Visible to MM-Wave Radiation (AGARD-CP-542)*. Neuilly sur Seine, France: AGARD, 1993, 195 pages.

[5] S. Kidder, M. Goldberg, R. Zehr, M. DeMaria, J. Purdom, C. Velden, N. Grody, and S. Kusselson, "Satellite analysis of tropical cyclones using the Advanced Microwave Sounding Unit (AMSU)," *Bull. AMS*, vol. 81, no. 6, pp. 1241–1259, Jun. 2000.

[6] K. Brueske and C. Velden, "Satellite-based tropical cyclone intensity estimation using the NOAA-KLM series Advanced Microwave Sounding Unit (AMSU)," *Mon. Wea. Rev.*, vol. 131, no. 4, pp. 687–697, Apr. 2003.

[7] K. Bessho, M. DeMaria, and J. Knaff, "Tropical cyclone wind retrievals from the Advanced Microwave Sounding Unit: Application to surface wind analysis," *J. Appl. Meteorol. Clim.*, vol. 45, no. 3, pp. 399–415, Mar. 2006.

[8] J. Halverson, J. Simpson, G. Heymsfield, H. Pierce, T. Hock, and L. Ritchie, "Warm core structure of Hurricane Erin diagnosed from high altitude dropsondes during CAMEX-4," *J. Atmos. Sci.*, vol. 63, no. 1, pp. 309–324, Jan. 2006.

[9] A. Gasiewski, J. Barrett, P. Bonanni, and D. Staelin, "Aircraft-based radiometric imaging of tropospheric temperature and precipitation using the 118.75 GHz oxygen resonance," *J. Appl. Meteorol.*, vol. 29, no. 7, pp. 620–632, Jul. 1990.

[10] P. Bauer and A. Mugnai, "Precipitation profile retrievals using temperature-sounding microwave observations," *J. Geophys. Res.*, vol. 108, no. D23, p. 4730, 2003.

[11] P. Bauer, E. Moreau, and S. Di Michele, "Hydrometeor retrieval accuracy using microwave window and sounding channel observations," *J. Appl. Meteorol.*, vol. 44, no. 7, pp. 1016–1032, Jul. 2005.

[12] D. Staelin and F. Chen, "Precipitation observations near 54 and 183 GHz using the NOAA-15 satellite," *IEEE Trans. Geosci. Remote Sens.*, vol. 38, no. 5, pp. 2322–2332, Sep. 2000.

[13] F. W. Chen and D. Staelin, "AIRS/AMSU/HSB precipitation estimates," *IEEE Trans. Geosci. Remote Sens.*, vol. 41, no. 2, pp. 410–417, Feb. 2003.

[14] V. Jamnejad, A. L. Riley, and P. T. Swindlehurst, "Reflector antenna systems for the High Altitude MMIC Sounding Radiometer (HAMSR)," in *Proc. IEEE Aerosp. Conf.*, 2000, vol. 5, pp. 113–117.

Shannon T. Brown (S'02–M'05) received the B.S. degree in meteorology from The Pennsylvania State University, University Park, and the M.S. degree in atmospheric science and Ph.D. degree in geoscience and remote sensing from the University of Michigan (UMich), Ann Arbor, in 2005.

He is a Senior Engineer with the Microwave Advanced Systems Section, NASA Jet Propulsion Laboratory (JPL), California Institute of Technology, Pasadena. His research interests include microwave radiometer calibration and geophysical algorithm development for both passive and active sensors. He has been involved with the spaceborne Topex and Jason Microwave Radiometers, the WindSat Polarimetric Radiometer, and the Jason follow-on Advanced Microwave Radiometer. He is currently the Instrument Scientist for the NASA Juno Microwave Radiometer.

Dr. Brown was the recipient of a NASA Group Achievement Award in 2004 for his contribution to the UMich/Goddard Space Flight Center Lightweight Rainfall Radiometer, the NASA Exceptional Achievement Medal in 2008, and the JPL Lew Allen Award in 2010.

Bjorn Lambrigtsen, photograph and biography not available at the time of publication.

Richard F. Denning (SM'09) received the B.S. degree from Pasadena City College, Pasadena, CA, in 1961.

After graduation, he joined the NASA Jet Propulsion Laboratory (JPL), California Institute of Technology, Pasadena, building and integrating instruments on the early Mariner, OGO, and Pioneer spacecraft, as well as the Apollo Lunar Surface Experiment Package. Since 1973, he has been designing and fielding scientific instruments, both ground-based and airborne, for the remote sensing of the Earth's atmosphere. He is currently a Senior Engineer with Microwave Systems Technology Group, JPL, California Institute of Technology.

He is a member of the IEEE Geoscience and Remote Sensing Society.

Todd Gaier, photograph and biography not available at the time of publication.

Pekka Kangaslahti, photograph and biography not available at the time of publication.

Boon H. Lim received the B.S. and M.S. degrees in electrical engineering and the Ph.D. degree in geoscience and remote sensing from the University of Michigan (UMich), Ann Arbor, in 1999, 2001, and 2008, respectively.

He was a Staff Engineer with the Space Physics Research Laboratory, UMich, from 2002 to 2003. He was a Graduate Student Research Assistant with the Remote Sensing Group, UMich, from 2004 to 2008, where his research involved microwave remote sensing calibration and instrumentation, including synthetic aperture radiometry. He is currently a Member of the Microwave Systems Technology Group, NASA Jet Propulsion Laboratory, California Institute of Technology, Pasadena.

He was the recipient of a NASA Group Achievement Award as a member of the Lightweight Rainfall Radiometer Instrument Team and of a NASA Earth System Science Fellowship from 2005 to 2008 to work on the "Development of a Geosynchronous Temperature and Humidity Sounder/Imager."

Jordan M. Tanabe received the B.S.E.E. degree from the University of California, San Diego, in 2007.

Since 2007, he has been with NASA Jet Propulsion Laboratory, California Institute of Technology, Pasadena, where he is currently an RF/Microwave Engineer with the Microwave Remote Sensing Instruments Section. He has been involved with ground-based water-vapor radiometers stationed at Goldstone DSN, Ka-band digital-beamforming radar digital back ends (GLISTIN-A and GLISTIN-IPY), and the High-Altitude MMIC Sounding Radiometer.

Alan B. Tanner received the B.S. and Ph.D. degrees in electrical engineering from the University of Massachusetts, Amherst, in 1985 and 1989, respectively. For his graduate work, he developed the Electronically Scanned Thinned Array Radiometer for soil-moisture measurements and the Stepped Frequency Microwave Radiometer for hurricane-wind-speed detection.

He is a Principal Engineer with the NASA Jet Propulsion Laboratory, California Institute of Technology, Pasadena, where he has been employed since 1989. He has specialized in the design and calibration of microwave radiometers and scatterometers for the remote sensing of the Earth for the past 25 years. He has been the Lead System Engineer for the Geostationary Synthetic Thinned Array Radiometer, the Ultrastable Radiometer testbed (which formed the basis of the Aquarius and Juno radiometer designs), the Advanced Water Vapor Radiometers for the Cassini Gravitational Wave Experiment, the Airborne Cloud Radar (a 94-GHz scatterometer which preceded the CloudSat mission), and the Airborne Rain Mapping Radar (built for validation of the Tropical Rainfall Measurement Mission).